Composites: Part A 190 (2025) 108681

Contents lists available at ScienceDirect

Composites Part A

journal homepage: www.elsevier.com/locate/compositesa

Effect of fiber surface state on the thermomechanical and interfacial properties of in situ polymerized polyamide 6/basalt fiber composites

Martino Valentini [a], Olivier De Almeida [b], Markus Kakkonen [c,d], Gerhard Kalinka [e], Andrea Dorigato [a], Pasi Kallio [d], Giulia Fredi [a,*]

[a] University of Trento, Department of Industrial Engineering and INSTM Research Unit, Via Sommarive 9, 38123 Trento, Italy
[b] Institut Clément Ader, Université de Toulouse, CNRS UMR 5312, IMT Mines Albi, UPS, INSA, ISAE-SUPAERO, Campus Jarlard, 81013, Albi, France
[c] Fibrobotics Oy, Korkeakoulunkatu 1 33720 Tampere Finland
[d] Faculty of Medicine and Health Technology, PO Box 589, Tampere University, FI-33014, Finland
[e] BAM Federal Institute for Materials Research and Testing, Department 5.3 Polymer Matrix Composites, Unter den Eichen 87, 12205 Berlin, Germany

ARTICLE INFO

Keywords:
Anionic polyamide 6
Reactive thermoplastics
Basalt fibers
Microdebonding
Fiber push out
Short beam shear test

ABSTRACT

This study investigates the thermomechanical properties and interfacial adhesion of novel in-situ polymerized anionic polyamide 6 (aPA6) composites reinforced with basalt fibers (BF). The impact of different BF surface states - as-received (BFa), ethanol-washed (BFw), and thermally desized (BFu) – on composite performance is examined through a comprehensive approach. For the first time, anionic PA6/BF composites with very low residual monomer content were successfully produced via thermoplastic resin transfer molding (tRTM). The PA6/BFw composites exhibited the highest interlaminar/interfacial shear strength in short beam shear test (52 ± 8 MPa) and fiber push out test (34 ± 11 MPa) tests. Fiber microdebonding test, performed only on PA6/BFw, yielded a low interfacial shear strength (12 ± 4 MPa), which was attributed to droplet porosity resulting from concurrent polymerization and crystallization. Thermal desizing significantly deteriorated interfacial strength (19.6 ± 1.2 MPa in short beam shear test). This multi-technique characterization provides insights into optimizing the fiber–matrix adhesion in these advanced thermoplastic composites.

1. Introduction

Reactive thermoplastics, in which a reactive mixture of monomers and catalysts is transferred into a mold where polymerization occurs, have gained considerable attention because of their numerous advantages over conventional thermoplastic and thermosetting systems [1,2]. Unlike traditional thermoplastics, the low viscosity of the reactive mixture allows it to effortlessly infiltrate dry reinforcements to produce near-net-shape components with fast processing times and an enhanced filler/matrix interfacial interaction [3,4]. Unlike thermosets, reactive thermoplastics can be reprocessed, post-thermoformed, and recycled and exhibit superior impact resistance, toughness, and damage tolerance, making them well suited for demanding structural applications [5–7]. Among the most promising reactive thermoplastics is anionic polyamide 6 (PA6). PA6 has garnered significant interest for use in composites owing to its good mechanical properties, chemical resistance, and thermal stability. The byproduct-free, anionic ring-opening polymerization (aROP) process of ε-caprolactam (ε-CL) in the presence of continuous reinforcements offers the aforementioned advantages over conventional melt processing techniques, as well as the potential for enhanced thermomechanical properties [8]. The aROP process occurs at a temperature well below the melting point of PA6 (~221 °C), resulting in a polymer with a low content of low-molar-mass portions and high crystallinity degree [9,10].

Among the available reinforcing fibers that can be combined with anionic PA6, basalt fibers (BFs) have emerged as a promising reinforcement in composite structures thanks to their exceptional mechanical and chemical properties [11,12]. BFs, derived from molten basalt rock, exhibit high tensile strength (~2.8 GPa), excellent thermal stability (−200 °C/600 °C), and remarkable resistance to corrosion and chemical degradation. With a density comparable to that of glass fibers (~2.7 g/cm^3) and a higher elastic modulus (90 GPa vs. 76 GPa), basalt fibers offer an attractive balance between performance and cost-effectiveness [13–15]. Furthermore, their natural origin and eco-

* Corresponding author.
E-mail address: giulia.fredi@unitn.it (G. Fredi).

https://doi.org/10.1016/j.compositesa.2024.108681
Received 23 October 2024; Received in revised form 2 December 2024; Accepted 20 December 2024
Available online 22 December 2024

friendly production process make them a sustainable alternative to traditional synthetic fibers [16,17]. The inherent fire resistance and low thermal conductivity of basalt fibers also contribute to their growing appeal in various industrial applications, particularly in environments where thermal management and fire safety are critical considerations [18]. Owing to these interesting properties, BFs have been used in combination with high-performance thermoplastic and thermosetting polymer matrices (e.g., epoxies) to produce polymer composites for various structural and non-structural applications, as well as with concretes and asphalts for applications in civil engineering [19–22]. Therefore, in situ anionic polymerization of PA6/BF composites offers significant advantages including a potentially enhanced fiber–matrix interfacial adhesion, improved mechanical properties, better fiber distribution, reduced void content, and superior thermal and chemical resistance and gas barrier properties thanks to the higher matrix crystallinity. These advanced composites may find applications in diverse sectors such as automotive (structural and body components), construction (reinforcement bars and panels), industrial equipment (pump housings and conveyor components), and sports/recreation (bicycle frames and protective equipment), leveraging their exceptional strength, lightweight nature, and multifunctional performance characteristics.

Despite the interesting properties of anionic PA6 and basalt fibers, no successful trials for preparing PA6/BF composites through in situ polymerization can be found in the open scientific literature. To the best of the authors' knowledge, the only reported attempt is that described by Alfonso et al. [23,24]. However, that trial was unsuccessful since the degree of conversion was very low, likely due to the presence of moisture in the reactants, which is well-known to inhibit the anionic polymerization of ε-CL [25]. By implementing rigorous moisture control techniques, including vacuum storage of reactants, careful fiber drying, and controlled premixing temperatures, we successfully overcame the critical moisture challenge that previously hindered composite preparation. Hence, for the first time, in this work we describe the successful preparation of anionic PA6/BF composites with very low residual monomer content.

When studying new fiber/matrix combinations, it is fundamental to investigate and optimize their interactions. In the field of continuous fiber composites, several techniques have been developed that operate at both the individual fiber and laminate levels. However, the debate as to which method is the most precise, reliable, and relevant is still ongoing [26]. At the fiber level (microscale), prominent methods include microbond/microdebonding, single fiber pull-out, single-fiber fragmentation, and micro-indentation/fiber push-out/push-in tests [27]. These techniques offer the advantage of isolating the fiber–matrix interaction, allowing for the precise measurement of interfacial properties. Microdebonding and fiber pull-out tests, although versatile in their applicability to various fiber–matrix combinations, are limited by the small scale, possible unrepresentativeness of the specimens, and difficulty in accurately assessing droplet geometry and size[26]. To address this last drawback, alternative methods have been proposed, such as the cylinder test [28]. The single-fiber fragmentation test provides valuable insights into the failure process, particularly in transparent matrices, but it requires specific matrix properties. The push-out test allows for in-situ measurement in the actual composite environment, although it presents challenges in observing the failure mode [29]. At the laminate level (mesoscale), methods such as short-beam shear (SBS), Iosipescu shear, and [±45°] tensile tests offer a more holistic assessment of interfacial properties within the composite structure [30]. However, these laminate-level tests, while providing data more representative of the bulk composite behavior, may be influenced by factors beyond the fiber–matrix interface. The diversity of these techniques, each presenting its own set of advantages and limitations, underscores the complexity of fiber–matrix adhesion characterization, suggesting that a comprehensive approach utilizing multiple methods may yield the most robust understanding of the interfacial properties in continuous fiber composites.

The fiber/matrix interfacial adhesion in anionic PA6 composites has been characterized through various experimental techniques, with SBS testing being the most prominent method. Van Rijswijk et al. [31] utilized SBS to investigate the impact of processing temperature and activator type on interfacial bonding in glass fiber/aPA6 composites. Their results revealed a strong dependence of interlaminar shear strength (ILSS) on the processing conditions, with values ranging from 50 to 80 MPa. Teuwen et al. [32] further explored the effects of post-polymerization (sometimes called "cure") time and annealing on ILSS in similar composites, demonstrating that optimized parameters could significantly enhance interfacial properties. More recently, Shim and Park [33] applied SBS testing to evaluate the performance of carbon fiber/aPA6 composites produced by a novel single-stream thermoplastic resin transfer molding (tRTM) process and reported ILSS values of 40–50 MPa. Micromechanical tests such as fiber push-out have been instead applied by Haspel et al. [34] to glass fiber/aPA6 composites. Their study revealed an average interfacial shear strength (IFSS) of 27.2 MPa and considerable variability between samples. Finally, microdebonding/pull out tests were performed by Sun et al. [35] to evaluate the IFSS in carbon fiber/aPA6 composites. However, their method of depositing matrix droplets by dissolving anionic PA6 in a solvent and subsequent drying likely altered the crystallinity of the matrix and disrupted any transcrystalline regions [36] that would typically form at the fiber–matrix interface during in-situ polymerization, potentially leading to results that did not accurately represent the true interfacial properties of the composite. In contrast, the work of Revol et al. [37] stands out as a more representative approach for anionic PA6 systems. The authors wetted the fibers with a reactive mixture containing ε-CL and catalysts, forming droplets that polymerized directly on the fiber surface. An IFSS of 20 ± 3 MPa has reported for glass fibers and 12 ± 3 MPa for viscose fibers. However, the reported degree of conversion of polymerized droplets was quite low, ranging between 66 and 73 %. Despite the importance of accurately measuring the fiber/matrix interaction, the large uncertainty brought about by any of the mentioned techniques, and the peculiarity of anionic PA6 in terms of polymerization and crystallization, a study comparing meso- and microscale interface testing techniques on the same anionic PA6-matrix composites was not found in the open scientific literature.

Hence, this study aims to investigate the microstructural, thermomechanical, and interfacial properties of in situ polymerized anionic PA6 composites reinforced with continuous basalt fibers (BFs). Specifically, the focus is on understanding how different surface treatments of basalt fibers (i.e., as-received, ethanol-washed, and thermally desized) affect the polymerization of PA6, the interfacial properties, and ultimately the overall performance of the composites. To achieve this goal, we employed a comprehensive multitechnique approach. First, the basalt fibers were treated and characterized, and then, for the first time, PA6/BF composites were successfully produced via tRTM. The microstructural, thermal, mechanical, and interfacial properties of the composites were then evaluated. Finally, to assess the fiber/matrix interfacial adhesion as a function of the BF surface state, three complementary techniques have been compared, namely short beam shear (SBS), fiber push-out (FPO), and fiber microdebonding (FMD) tests. This multifaceted approach allows us to gain a comprehensive understanding of the interfacial behavior at different scales and under various stress states, providing valuable insights into the complex interplay between fiber surface treatment, matrix properties, and interfacial adhesion in these advanced thermoplastic composites.

2. Materials and methods

2.1. Materials

ε-caprolactam (ε-CL), with commercial name AP-Nylon® Caprolactam, was used with the initiator Bruggolen C10® (17–19 % sodium

caprolactamate in ε-CL) and the activator Bruggolen C20P® (blocked diisocyanate, 17 % N=C=O content blocked with ε-CL). These three products were kindly provided by Brüggemann GmbH (Heilbronn, Germany) and stored in dry conditions until use. Plain-weave basalt fiber fabric BAS220P® (density of the fibers = 2.67 g/cm^3, areal density of the fabric = 220 g/m^2) was purchased from Basaltex NV (Wevelgem, Belgium). According to the producer, the surface sizing is made by (3-glycidyloxypropyl)trimethoxysilane.

2.2. Sample preparation

2.2.1. Surface treatment of the basalt fibers

Basalt fibers were used both as-received and after two treatments, performed to modify their surface state. The first consisted of a simple rinsing of the fabric with ethanol, by dipping them in ethanol three times for a duration of 15 s each. This treatment was performed to remove the surface impurities. The second consisted of a thermal treatment in an oven at 400 °C for 4 h, performed to remove the silane sizing. The desizing parameters were selected following a procedure described in the literature [17] and confirmed by a preliminary thermogravimetric analysis (TGA) test on the as-received fibers, which highlighted the optimal degradation temperature. The specific treatment performed on the basalt fabric will be, from now on, designated by the following labels: BFa for as-received basalt fibers, BFw for basalt fibers washed with ethanol, and BFu for thermally unsized basalt fibers.

2.2.2. Preparation of the PA6/BF composites

The sample preparation route is schematized in Fig. 1. ε-CL was melted in a three-necked round bottom flask and stirred at 110 °C for 45 min under N_2 flux. C10 was then added in a concentration of 2.20 phr (parts per hundred resin, i.e., grams every 100 g of ε-CL) and the mixture was then stirred for 30 more minutes under N_2 flux. In the end, C20P was added in the concentration of 1.50 phr and the mixture was stirred for 90 s, after which the reactive mixture was transferred, with the pressure of nitrogen gas, in a preheated mold through preheated Teflon tubes. The mold, made of aluminum, had an inner chamber of 150 × 160 × 2 mm^3 and already contained 8 plies of BF fabric with areal dimensions of 150 × 160 mm^2, carefully dried at 80 °C for 2 h (to prevent polymerization inhibition due to residual moisture) and weighed before insertion in the mold. After the transfer and complete filling of the mold, the reactive mixture was left polymerizing in the mold around the BF at 165 °C for 30 min. Since the demolding time has been shown to affect the total conversion [38], this time has been kept constant across all the compositions to ensure full and homogeneous polymerization. Then, the temperature was switched off and the sample was demolded. The produced specimens were stored in a dry environment (under dry silica gel) until testing. The prepared specimens are listed in Table 1.

The optimum concentration of C10 and C20P in ε-CL, as well as the optimum polymerization temperature, depend on many factors, such as the dimension and size of the cast parts, processing temperatures, desired reaction time, and target physical properties [39]. In this work, the concentrations of C10 and C20P of 2.20 phr and 1.50 phr, respectively, and the polymerization temperature of 165 °C were selected because, according to a previous optimization [40], they allow the production of a PA6 matrix with the best possible combination of elastic modulus, tensile strength, and strain at break and they also result in a polymerization rate slow enough to allow the complete filling of the mold before the viscosity increases excessively.

Table 1
List of prepared samples with nominal composition and processing.

Sample	Matrix	Polymerization temperature (°C)	Composition	Reinforcement	# plies
PA6/BFa	aPA6	165	2.20 phr C10; 1.50 phr C20P	As-received BF	8
PA6/BFw	aPA6	165	2.20 phr C10; 1.50 phr C20P	BF washed with ethanol	8
PA6/BFu	aPA6	165	2.20 phr C10; 1.50 phr C20P	Thermally desized BF (400 °C–4 h)	8

Phr = parts per hundred resin, i.e.*, grams every 100 g of monomer.*

2.3. Characterization

2.3.1. Characterization of the basalt fibers

The lateral surface of BFa, BFw, and BFu were observed via field emission scanning electron microscopy (FE-SEM). The specimens were placed on a conductive tape over a metallic stub and then subjected to Pt-Pd sputtering. Micrographs were taken at different magnifications with a Zeiss SUPRA 40 FE-SEM (Carl Zeiss Industrielle Messtechnik GmbH, Oberkochen, Germany).

Thermogravimetric analysis (TGA) was carried out on BFa to measure the optimal desizing temperature of BF. TGA was performed via the IR thermobalance Mettler TG 50 (Mettler Toledo Inc., Columbus, Ohio, USA). Specimens of approx. 30 mg were subjected to a thermal ramp between 30 °C and 700 °C with a heating rate of 10 °C/min, under a constant nitrogen flux of 10 ml/min. The desizing temperature was chosen after the observation of the sizing degradation signal. The same test was also performed on BFw and BFu.

Tensile tests were performed on as-received fibers according to the standard ASTM C1557. Single fibers were attached to paper frames with a nominal gauge length (l_0) of 10, 20, or 30 mm, which was also the initial distance between the grips. The diameter of each fiber was measured with a light microscope Zeiss Axio Imager A1.m. (Carl Zeiss

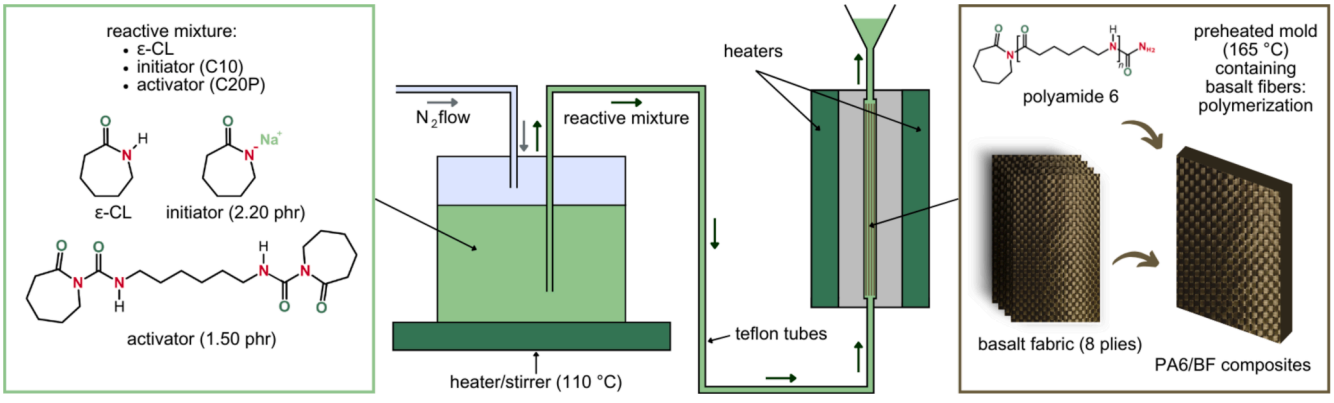

Fig. 1. Schematic of the lab-scale thermoplastic resin transfer molding setup for the preparation of anionic PA6/basalt fiber composites.

Industrielle Messtechnik GmbH, Oberkochen, Germany). Tests were performed with a universal electromechanical dynamometer Instron 5969 (Instron, Norwood, MA, USA) equipped with a 10-N load cell. The test was performed on at least 20 specimens for each l_0, at a strain rate of 0.05 min^{-1}. The test allowed the determination of the elastic modulus and the Weibull parameters, i.e., the shape factor or Weibull modulus m and the scale factor σ_0. The elastic modulus was determined as the inverse of the slope of the regression line of the plot elongation/force ($\Delta L/F$) versus initial length/cross-section (l_0/A). The Weibull parameters were determined via Eq. (1), as

$$ln\bar{\sigma}_x = ln\sigma_0 - \frac{1}{m}ln\frac{L_x}{L_0} + ln\Gamma\left(1+\frac{1}{m}\right) \quad (1)$$

where $\bar{\sigma}_x$ is the average experimental tensile strength of the fibers with length L_x (10 mm, 20 mm, or 30 mm) and Γ represents the gamma function. Hence, once set L_0 equal to 1 and plotted $ln\bar{\sigma}_x$ as a function of lnL_x, the linear regression has a slope equal to $-1/m$, and σ_0 can be determined from the intercept with the y-axis.

2.3.2. Characterization of the PA6/BF composites

The cryofractured surface of the prepared composites was analyzed via FE-SEM in the same way as what has been reported for basalt fibers.

TGA test was performed with the same equipment and testing parameters described for the characterization of the BF. For the composites, this test allowed the determination of the temperatures corresponding to a mass loss of 1 wt%, 3 wt%, and 5 wt% ($T_{1\%}$, $T_{3\%}$, $T_{5\%}$), the onset temperature for degradation using the tangent method (T_{onset}), the weight fraction lost at 250 °C, corresponding to the degradation temperature of residual ε-CL ($m_{L,250}$), the residual mass at 700 °C (R_c), and the degradation temperature (T_d), at the maximum of the first derivative of the TGA thermogram (DTG). A conversion degree according to TGA results (CD_{TGA}) was then calculated via Eq. (2), as

$$CD_{TGA} = \left(1 - \frac{m_{L,250}}{w_{f,TGA}}\right)\cdot 100, \quad (2)$$

where $w_{f,TGA}$ is the fiber weight fraction calculated by knowing the residual masses of the matrix (R_m) and the fibers (R_f) via Eq. (3), as

$$w_{f,TGA} = \frac{R_c - R_m}{R_f - R_m}. \quad (3)$$

Differential scanning calorimetry (DSC) was performed via a Mettler DSC 30 (Mettler Toledo Inc.). Specimens of approx. 30 mg were sealed in aluminum crucibles and subjected to a heating/cooling/heating cycle between 0 °C and 250 °C at ±10 °C/min, under a constant nitrogen flow of 100 ml/min. The tests allowed measuring the melting and crystallization temperatures (T_m and T_c) and enthalpies (ΔH_m and ΔH_c) and calculating the degree of crystallinity (χ) of the polymerized PA6 fraction via Eq. (4), as

$$\chi = \frac{\Delta H_m - \Delta H_{cc}}{(1 - w_{f,TGA})\cdot CD_{TGA}\cdot \Delta H_0}\cdot 100, \quad (4)$$

where ΔH_{cc} is the cold crystallization enthalpy and ΔH_0 is the theoretical melting enthalpy of a 100 % crystalline polymer, equal to 230 J/g for the α form of PA6 [41].

The experimental density of the prepared composites (ρ_{exp}) was obtained via Archimedes' balance (ASTM D792) by weighing the samples in ethanol (ρ_{EtOH} = 0.80458 g/cm^3, measured at 20 °C) with a Gibertini E42 analytical balance (Gibertini, Novate Milanese (MI), Italy). This data allowed the calculation of the volume fraction of voids (ϑ_v), by knowing the weight fractions and densities of the matrix and fibers in the prepared composites. The weight composition was determined in two ways, i.e., by measuring the weight fraction of fibers via TGA ($w_{f,TGA}$), as previously described, and by calculating the ratio between the total mass of BF introduced in the mold and the final mass of each composite ($w_{f,mass}$). The density of the neat PA6 was measured with the same Archimedes's balance technique used for the composites, while the density of BF fibers was taken from the producer's datasheet. These data allowed the calculation of the theoretical density of the prepared composites (ρ_{th}).

The thermal diffusivity and conductivity of the prepared composites were determined via a light flash analyzer LFA 467 (Netzsch Holding Gmbh, Selb, Germany). Tests were performed at 25 °C on discoidal specimens with a diameter of 12.7 mm, coated with a graphitic spray on both sides. At least two specimens per composition were tested and at least five pulses were performed on each specimen. Data were analyzed with the embedded software Proteus® (V. 8.0.2) by applying a standard model with linear baseline and numerical pulse correction. These tests allowed the direct measurement of the thermal diffusivity (α). The specific heat capacity (c_P) was determined using Pyroceram® 9606 as the reference material. Then, the thermal conductivity at 25 °C (λ) was calculated via Eq. (5), as

$$\lambda = \alpha\cdot\rho\cdot c_P \quad (5)$$

where ρ is the experimental density (at 23.0 °C).

Dynamical mechanical thermal analysis (DMTA) was performed to investigate the material response to stress and temperature and to capture the thermal behavior of the prepared PA6/BF composites around the glass transition. DMTA tests were performed via the DMA Q800 (TA Instruments, Inc., New Castle, DE, USA) in single cantilever mode (span length = 17.5 mm), with a strain amplitude of 0.05 % applied at a frequency of 1 Hz. The test was performed in the temperature range of 0–170 °C with a heating rate of 3 °C/min. The storage modulus (E'), loss modulus (E''), and loss factor ($tan\delta$) were measured as a function of temperature. The glass transition temperature was evaluated at the peak of E'' ($T_{g,E''}$).

Three-point bending tests were performed under quasi-static conditions with an Instron 5969 dynamometer equipped with a 10-kN load cell, following the standard ASTM D790. The tested specimens had a dimension of 150 × 10 × 2 mm^3, the testing speed was set at 7.2 mm/min to reach the strain rate prescribed by the standard, and the span length was set at 100 mm (span-to-thickness ratio = 50). The test was performed until the sample failed or until a strain of 7 %. The test allowed the measurement of the flexural modulus (E_f), strength (σ_{fM}) at the maximum load, strain at the maximum load (ε_{fM}), and strain at break (ε_{fb}). The test was performed on at least five specimens per sample. The fracture surfaces were analyzed with SEM, with the same equipment described for the BF, to qualitatively analyze the fiber/matrix adhesion and its variation with the fiber surface treatment. Statistical analysis of the results of the thee point bending test was performed using R Studio v. 2023.12.1 (RStudio, Inc., Boston, MA, USA). To assess the effects of the experimental factor (surface state of the BFs), a one-way analysis of variance (ANOVA) was conducted. In cases where the ANOVA revealed statistically significant differences, Tukey's honest significant difference (HSD) post-hoc test was employed to identify specific group comparisons that were significantly different from one another. All statistical tests were evaluated at a significance level of 0.05.

2.3.3. Investigation of the fiber/matrix interfacial adhesion

The investigation of the interfacial adhesion between PA6 and BF was performed through three tests, i.e., short beam shear, fiber push out, and microdebonding tests, schematized in Fig. 2. Short-beam shear (SBS) tests were conducted with an Instron 5969 dynamometer equipped with a 10-kN load cell, following the standard ASTM D2344. Specimens with dimensions of 15 × 5 × 2 mm^3 were tested at 1 mm/min with a span length of 8 mm (span-to-thickness ratio = 4) to maximize the shear stresses and favor delamination. The test allowed the determination of the short beam strength (F^{sbs}), calculated via Eq. (6), as

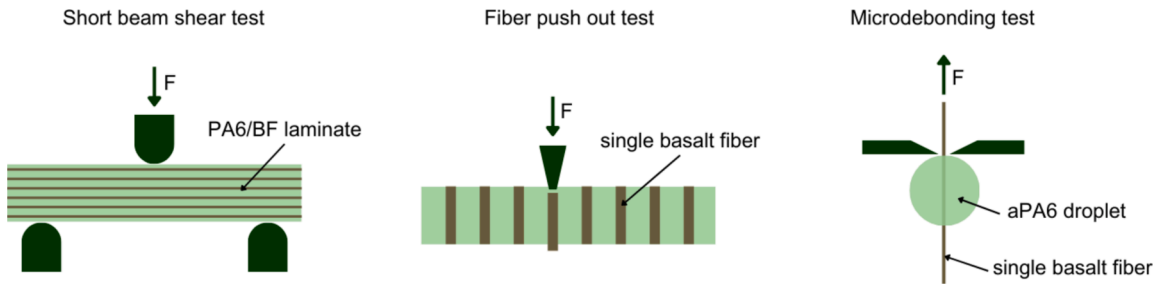

Fig. 2. Schematic of the three tests performed to characterize the interfacial adhesion between PA6 and basalt fibers.

$$F^{SBS} = 0.75 \cdot \frac{P_m}{b \cdot h} \tag{6}$$

where P_m is the maximum load, b the specimen width, and h the specimen thickness.

In the short beam test, failures are generally dominated by the properties of the matrix and/or the interlaminar properties and can therefore give some information on the fiber/matrix adhesion. However, to better understand the adhesion, two micromechanical tests were performed, i.e., fiber push-out and microdebonding.

For the single fiber push-out tests (FPO), the composites were cut into 3 × 10 mm^2 specimens and embedded in epoxy resin. After curing the resin, slices with a thickness of approx. 200–300 μm were cut off using an inboard saw (Leica). The discs were then ground to a thickness of 20–25 μm with an EXAKT 400CS polishing machine (Exakt) and were then placed in a lab-made push-out testing device. Here, the fibers were individually pushed out under a microscope with an indenter needle (steel straight circular cone). The test speed was 0.2 μm/s, while the force was recorded with a 50 N force sensor (Kistler 9207). The force–displacement relationship was recorded and the shear strength (F^{SFPO}) was calculated as the maximum force (P_m) per fiber surface area, i.e., according to Eq. (7), as

$$F^{SFPO} = \frac{P_m}{2\pi r_f l_f} \tag{7}$$

where r_f is the fiber radius and l_f is the fiber embedded length. A detailed description of the experimental procedure is reported elsewhere [42].

The fiber microdebonding (FMD) tests were conducted using a FIBRObond system (Fibrobotics Oy, Finland) equipped with a 1 N load cell. Before testing, the embedded length of each droplet was automatically measured by the FIBRObond apparatus. Microblades were then positioned at the tip of the droplets to initiate debonding. During the microdebonding process, force data were continuously recorded at a displacement rate of 4 μm/s. A detailed explanation of the device and the experimental procedure can be found in Laurikainen et al. [43]. Three fibers with at least 27 droplets on each were tested with this method.

To prepare the samples for the test, ε-CL and C10 (2.20 phr) were melted in a double-walled beaker at 90 °C. After full melting of ε-CL and C10 and mixture homogenization, C20P (1.50 phr) was added and the mixture was stirred for 1 min. The reactive mixture was then transferred into a beaker immersed in a sand bath at 160 °C. Then, droplets of reactive mixture were deposited onto single basalt fibers, which had been previously fixed onto an aluminum frame. Then the frame with all fibers and droplets was quickly transferred into a lab-made small oven to complete polymerization at 160 °C for 15 min. This procedure, which allowed depositing up to 30 microdroplets onto a single BF, was entirely performed in a glovebox inflated with nitrogen gas, and the preparation started only when the inner relative humidity decreased below 1 %, to prevent deactivation of the initiator due to the reaction with moisture. The deposited droplets were observed with a FEI Nova NanoSEM 450. Because of the complexity of the sample preparation process, the test was performed only on the basalt fibers washed with ethanol (BFw) because they were those that seemed to show a better fiber/matrix interfacial adhesion, given the results of the previous test.

Statistical analysis of the results of the interfacial characterization was performed using R Studio version 2023.12.1 (RStudio, Inc., Boston, MA, USA). To assess the effects of the two considered experimental factors (surface state of the BFs, i.e., BFa, BFw, and BFu, and type of test, i.e., SBS, FPO, and FMD), a two-way ANOVA was conducted. In cases where the ANOVA revealed statistically significant differences, Tukey's honest significant difference (HSD) post-hoc test was employed to identify specific group comparisons that were significantly different from one another. All statistical tests were evaluated at a significance level of 0.05.

3. Results and discussion

3.1. Characterization of basalt fibers

Microscopic analysis reveals distinct surface characteristics among differently treated basalt fibers. Dirt and surface impurities, evident in as-received fibers (BFa, Fig. 3a), are instead absent in ethanol-washed fibers (BFw, Fig. 3b), which only display the sizing layer. Heat-treated fibers (BFu, Fig. 3c) exhibit perfectly smooth surfaces, indicating complete sizing removal, similar to what is reported in previous works [17]. The average fiber diameter is measured at 14.2 ± 1.2 μm, and the desizing treatment has a negligible impact on fiber diameter. While individual fibers show slight diameter variations along their length, as also confirmed by optical microscope measurements (not reported for brevity), more significant inconsistencies were observed between different fibers. This variability is attributed to the basalt fiber production process, as noted by Samper et al. [44].

The process and temperatures of sizing removal were studied more in-depth via thermogravimetry. TGA curves (Fig. 4) reveal distinct thermal behaviors across different temperature ranges. In the as-received fibers (BFa), a clear mass loss is observed between 350 °C and 500 °C, which corresponds to the thermal degradation of the sizing and other surface impurities. This loss is still observable, although to a lesser extent, in the BFw fibers and is notably absent in the heat-treated fibers (BFu). This suggests that the washing treatment is effective in removing surface impurities and preserving the sizing, while the thermal treatment successfully removes all the surface substances. Unfortunately, the employed instrument does not allow discrimination between the degradation of the sizing and that of the other surface impurities, and some drifts and other artifacts may be present in the results although a blank correction was performed. Nevertheless, these results align well with the technical datasheet specifications, which indicate a sizing content of 0.2 wt%. This also agrees with the total mass loss of the basalt fabric after the thermal treatment, measured with a balance. Based on these observations, the chosen desizing conditions of 400 °C for 4 h appear to strike an effective balance between the successful removal of the commercial sizing while minimizing excessive surface dihydroxylation [45], thereby preserving the fiber's surface chemistry.

Fig. S1 shows the results of the tensile tests on as-received BF. The

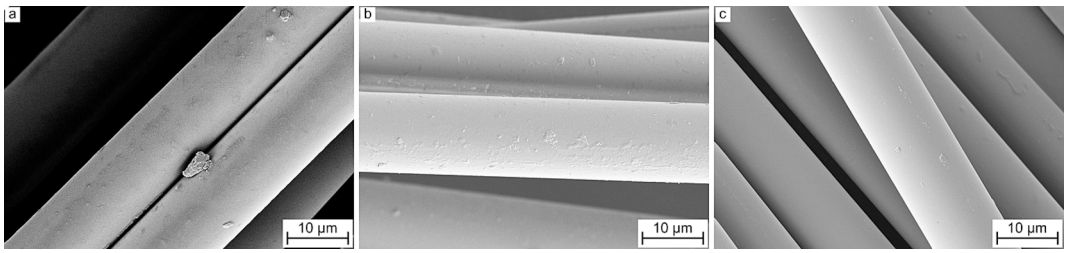

Fig. 3. SEM micrographs of the lateral surface of (a) as-received (BFa), (b) washed (BFw), and desized (BFu) basalt fibers.

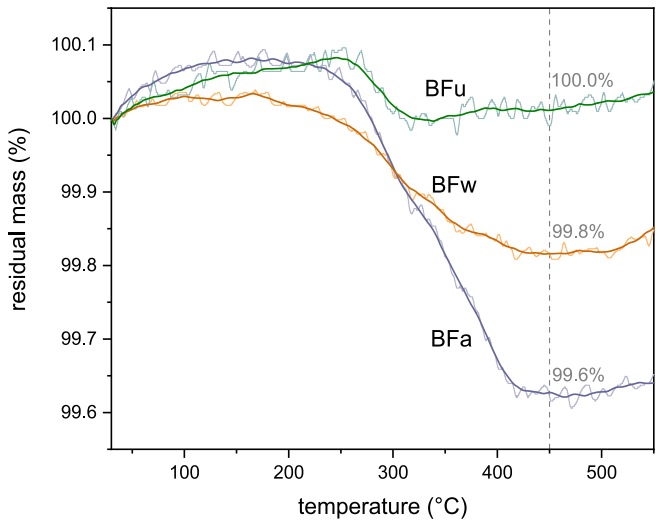

Fig. 4. TGA thermograms of the as-received (BFa), ethanol-washed (BFw), and desized (BFu) basalt fibers. Residual mass as a function of temperature. Experimental and smoothed data. The reported residual mass at 450 °C refers to the smoothed data.

stress–strain curve (Fig. S1a) is characterized by a linear elastic behavior up to a brittle failure. The experimental tensile strength, corresponding to the maximum stress values, ranges from 1.7 to 2.5 GPa and increases with a decrease in the initial fiber gauge length due to the increasing probability of critical defects, as expected from the weakest link theory [46,47]. The Young's modulus of BFa, calculated from the slope of the linear regression of the displacement/force vs. gauge length/area curve (Fig. S1b), was calculated as 75.2 GPa, in line with what is reported in the literature [48]. Moreover, the average tensile strength ranges from 1.7 to 2.5 GPa, decreasing with increasing gauge length. From these values, the Weibull parameters m and σ_0 result as 2.9 and 6.3 GPa, respectively. The resulting m value is generally lower than that reported in the literature for similar fibers, which denotes a strong variability of the tensile strenght. σ_0 is instead generally higher than what is found in the literature [11,12,49]. This denotes a considerable size sensitivity of the employed basalt fibers. The results of the characterization of as-received basalt fibers are reported in Table S1.

3.2. Characterization of PA6/BF composites

The role of the fiber surface state on the fiber/matrix interaction is very evident already from the SEM micrographs of the cryofractured cross-sections, reported in Fig. 5(a-f). The samples PA6/BFa (Fig. 5a,d) and PA6/BFw (Fig. 5b,e) exhibit substantial matrix residue on the fibers, indicating a mixed adhesive-cohesive fracture and enhanced fiber–matrix adhesion attributed to the presence of sizing. This effect is particularly pronounced in PA6/BFw, as observable from the cross-section in Fig. 5e, where the matrix demonstrates superior penetration between fibers and evident residues onto the fiber surface. In contrast, PA6/BFu samples display clean fiber surfaces (Fig. 5c) and extended pull-out (Fig. 5f), suggesting an almost completely adhesive fracture and, as expected, inferior interfacial adhesion.

Moreover, in PA6/BFa and PA6/BFw, localized regions of the matrix adjacent to the fibers show evidence of elongation and plasticization during fracture. This behavior contrasts sharply with the PA6/BFu composite, which displays a uniformly brittle fracture and considerable gaps between the fibers and the matrix. These differences may be attributed either to differences in the anionic PA6 matrix itself, which may polymerize and crystallize differently depending on the different fiber surface status, or to variations in the fiber/matrix adhesion. Now, we argue that this variable fracture pattern is almost entirely due to a different fiber/matrix interfacial strength, which promotes elongation and plasticization in the composites with sized fibers (PA6/BFa and PA6/BFw) and a fully brittle matrix fracture in the composite with desized fibers (PA6/BFu). In fact, the properties of the matrix do not vary considerably across the different composites, as is demonstrated hereafter with TGA, DSC, and DMTA tests.

Fig. 6(a,b) and Table 2 report the main results of thermogravimetric analysis (TGA), conducted to investigate the thermal stability and composition of the PA6/basalt fiber composites. The temperature at 1 % weight loss ($T_{1\%}$) of PA6/BFa and PA6/BFw is lower than that of neat PA6, likely due to the premature degradation of the fiber sizing and other surface impurities. On the other hand, PA6/BFu has a higher $T_{1\%}$ than neat PA6, and $T_{3\%}$ and $T_{5\%}$ are higher for all the prepared composites compared to the neat matrix. From the DTG (Fig. 6b), two main degradation peaks are observable (located at T_{d1} and T_{d2} in Table 2), which could be attributed to a bimodal distribution of the molecular weight, as observed in previous works [40]. The introduction of BF shifts the intensity balance between the two peaks towards the second, and the washing treatment seems to completely depress the first degradation peak, while it is still present both in PA6/BFa and PA6/BFu. This may be the signal of a different polymer chain architecture, a different crystallization process onto the basalt fibers, or a higher average molecular weight and a reduced polydispersity, although further analysis is needed to fully clarify this point. It is important to point out that the differences between the three composites in terms of peak intensity are, although not negligible, surely marginal, which contributes to the hypothesis that the properties of the matrix are not heavily affected by the fiber surface state.

It is also interesting to note that the introduction of BF does not decrease the conversion degree (CD_{TGA}), calculated from the mass loss at 250 °C, temperature at which all the residual monomer has degraded. As reported in Table 2, CD_{TGA} is always very high (>97.2 %) for all the prepared composites, regardless of the fiber surface treatment.

TGA also enabled the calculation of fiber and matrix mass percentages, as well as the volume fractions of fibers and voids in the composites. The results, presented in Table 3, show fiber weight fractions ($w_{f,TGA}$) of approx. 50–52 wt%, comparable across all the prepared composites and in good agreement with the values obtained from sample weighing ($w_{f,p}$). Notably, the void volume fraction was higher in the PA6/BFa composite (6.6 vol% vs. 1.4 vol% for PA6/BFw and 3.6 vol% for PA6/BFu), likely due to impurities on the fiber surface and its status as the first produced sample. However, the overall comparability of void

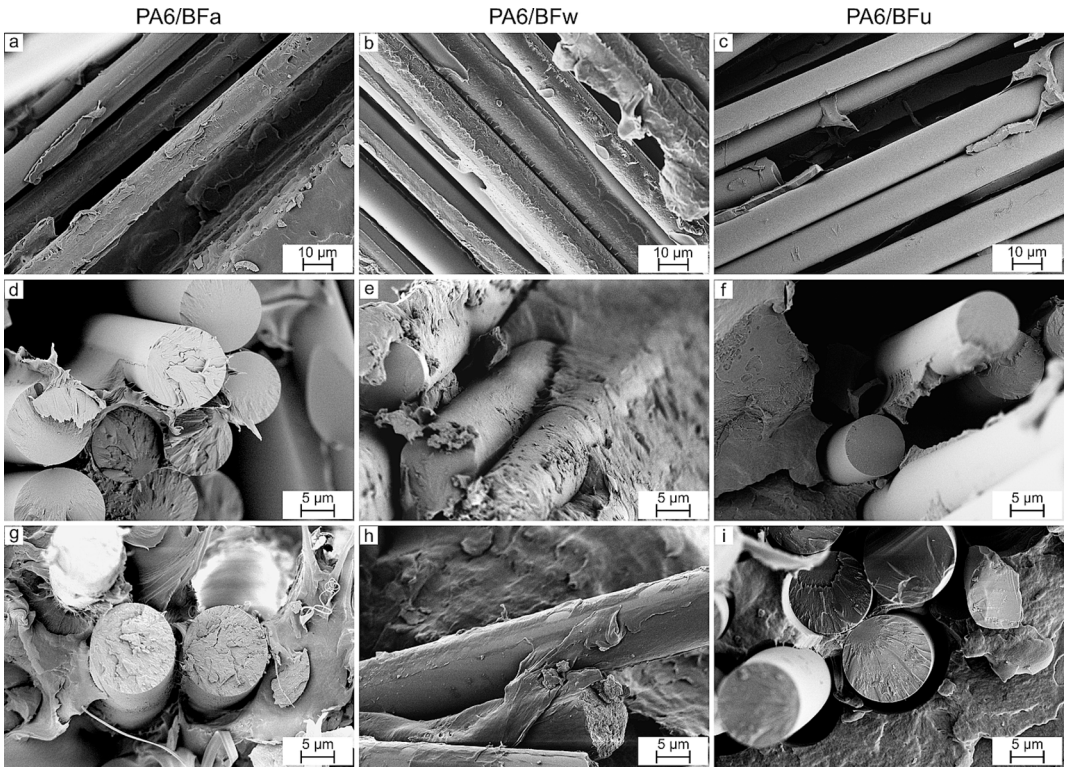

Fig. 5. SEM micrographs of the cryofractured cross-section of the prepared composites, evidencing sections along (a-c) and across (d-i) the fiber axis. (a,d,g) Composite with as-received fibers (PA6/BFa); (b,e,h) composite with washed fibers (PA6/BFw); (c,f,i) composite with thermally desized fibers (PA6/BFu).

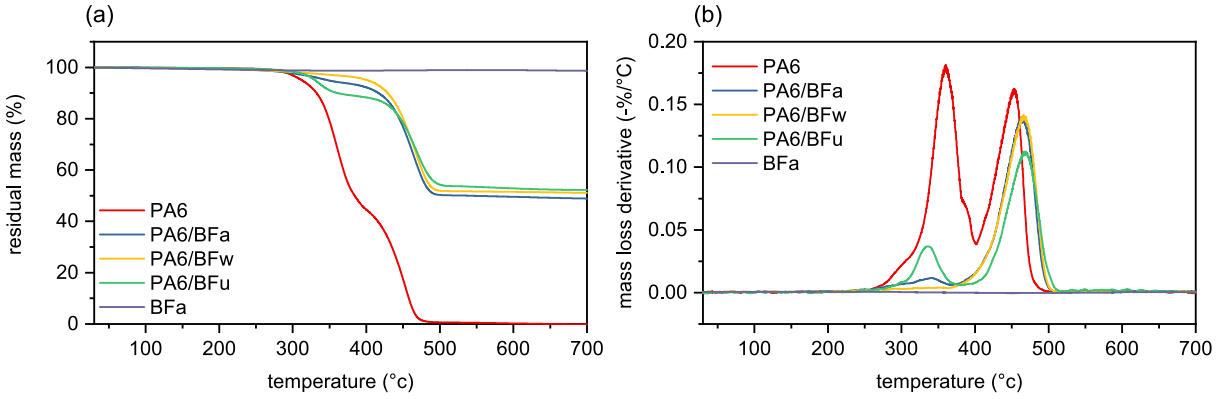

Fig. 6. TGA thermograms of the prepared composites, the neat PA6 matrix, and the as-received fibers. (a) Residual mass and (b) mass loss derivative (DTG) as a function of temperature.

Table 2
Main results of the TGA tests on the prepared composites.

Sample	$T_{1\%}$(°C)	$T_{3\%}$(°C)	$T_{5\%}$(°C)	T_{d1}(°C)	T_{d2}(°C)	R_c(wt%)	$m_{L,250}$(wt%)	CD_{TGA}(%)
PA6	273.1	299.1	312.3	360.0	452.8	0.0	0.5	99.5
PA6/BFa	230.2	304.8	345.1	336.4	466.0	49.6	1.4	97.2
PA6/BFw	242.3	354.9	401.6	352.0	466.3	51.1	1.1	97.7
PA6/BFu	280.6	318.3	330.3	336.0	468.0	52.8	0.6	98.7

$T_{1\%}, T_{3\%}, T_{5\%}$ = temperatures corresponding to a mass loss of 1 wt%, 3 wt%, and 5 wt%; T_{d1}, T_{d2} = degradation temperatures, corresponding to the two local maxima of the derivative thermogravimetry (DTG) curve; R_c = residual mass at the end of the test; $m_{L,250}$ = mass loss at 250 °C; CD_{TGA} = conversion degree measured via TGA data.

content and fiber volume fraction across samples allows for a meaningful comparison of mechanical properties.

The complex interplay between basalt fibers, their surface treatment, and the crystallization behavior of PA6 in the resulting composites was better investigated via DSC. Fig. 7(a–c) presents the DSC thermograms for the first heating, cooling, and second heating scans of the neat PA6 matrix and all the prepared composites. While the glass transition temperature (T_g) cannot be precisely determined, a slight inflection is

Table 3
Fiber weight and volume fraction, theoretical and experimental density, and porosity of the prepared composites.

Sample	$w_{f,TGA}$ (wt %)	$w_{f,mass}$ (wt %)	ρ_{th} (g/cm^3)	ρ_{exp} (g/cm^3)	ϑ_v (vol %)	ϑ_f (vol %)
PA6/BFa	50.3	47.7	1.604	1.495 ± 0.006	6.6	28.2
PA6/BFw	51.8	49.9	1.623	1.600 ± 0.024	1.4	31.5
PA6/BFu	52.8	50.1	1.636	1.581 ± 0.008	3.4	32.4

$w_{f,TGA}$ = weight fraction of fibers according to TGA tests; $w_{f,mass}$ = weight fraction of fibers measured by weighing the composites; ρ_{th} = theoretical density; ρ_{exp} = experimental density; ϑ_v = void volume fraction; ϑ_f = fiber volume fraction.

observed in the range of 40–55 °C, consistent with the expected T_g of PA6 [50–52]. The melting temperatures (T_m) in the first heating scan aligns with the expected melting of the α crystalline phase of PA6 (221 °C, see [53]) and is shifted to slightly higher temperatures in the composites (Table 4), likely due to the lower thermal conductivity of the composites compared to PA6, which depend on the insulating properties of basalt fibers [18]. The decrease in thermal conductivity with the addition of BF was also proved experimentally via LFA, for which the results are reported in the Supplementary Materials (Fig. S2). (SeeFig. 8.)

The crystallinity values derived from the first and second heating cycles differ significantly, indicating a strong influence of the production process on PA6 crystallization. In fact, in situ anionic polymerization of PA6 generally results in matrices with higher crystallinity, which can be further tuned by varying the processing parameters [40,54]. Notably, the PA6/BFu composite exhibits a higher crystallinity (45.0 %, see Table 4) during the first heating, suggesting that the presence of sizing may hinder PA6 crystallization. This observation aligns with the findings of Kim et al. [55] and Haspel et al. [34], who reported challenges in PA6 crystallization in the presence of sizing especially among densely packed fibers, due to poor chemical affinity and stoichiometric hindrance. However, the differences measured for these composites are quite modest, suggesting that the fiber surface states considered in this work do not alter considerably the crystallization behavior of the in situ polymerized PA6. However, further investigation is needed to fully clarify this aspect.

The glass transition of the PA6 in the prepared composites was better highlighted in DMTA tests, which also allowed the measurement of the viscoelastic parameters. The main results of DMTA tests are reported in Fig. 6 and Table 4. At low temperatures, the storage modulus (E') of the composites is comprised between 8.3 and 10.2 GPa, naturally higher than that of the matrix (2.8 GPa [40]). Notably, the E' of PA6/BFa is the lowest among the composites, likely due to a lower fiber volume fraction and a higher fraction of voids, as discussed before (see Table 3). For all the samples, a sharp decrease in E' is observed at around 50–60 °C, in accordance with the glass transition of the PA6 matrix, though the composites maintain higher E′ values compared to neat PA6 thanks to the presence of BF. Interestingly, the T_g, determined from the E'' peak (Table 4), is lower for PA6/BFa than for the neat PA6 matrix, possibly due to residual monomer or surface impurities acting as a plasticizer or weakened hydrogen bonding between polymer chains due to the presence of BF, as previously reported by Liang et al. for PA6/carbon fiber composites [56]. On the other hand, PA6/BFu and PA6/BFw show a higher T_g, likely because of hindered polymer relaxation attributed to a

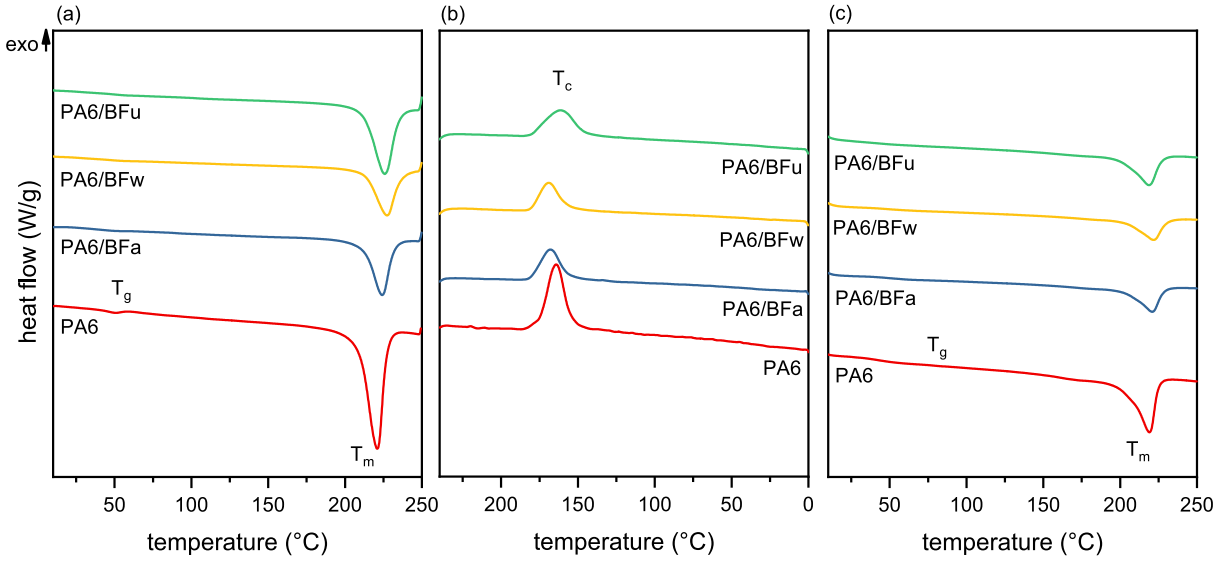

Fig. 7. DSC thermograms of the prepared composites and the neat PA6 matrix. (a) first heating scan; (b) cooling scan; (c) second heating scan.

Table 4
Main results of the DSC and DMTA test on the prepared composites and the neat PA6 matrix.

Sample	DSC T_{m1} (°C)	ΔH_{m1} (J/g)	χ_1 (%)	T_c (°C)	ΔH_c (J/g)	T_{m2} (°C)	ΔH_{m2} (J/g)	χ_2 (%)	DMTA $T_{g,E''}$ (°C)
PA6	220.7	95.7	41.8	165.6	57.2	217.7	60.1	26.3	66.5
PA6/BFa	222.2	47.3	42.6	169.4	32.7	219.8	33.9	30.5	63.0
PA6/BFw	224.4	42.5	39.2	171.1	30.1	219.7	30.9	28.5	73.3
PA6/BFu	221.7	48.2	45.0	167.5	28.9	219.0	30.3	28.3	72.4

T_{m1}, ΔH_{m1} = melting temperature and enthalpy (first heating scan); χ_1 = degree of crystallinity (first heating scan); T_c, ΔH_c = crystallization temperature and enthalpy (cooling scan); T_{m2}, ΔH_{m2} = melting temperature and enthalpy (second heating scan); χ_2 = degree of crystallinity (second heating scan).

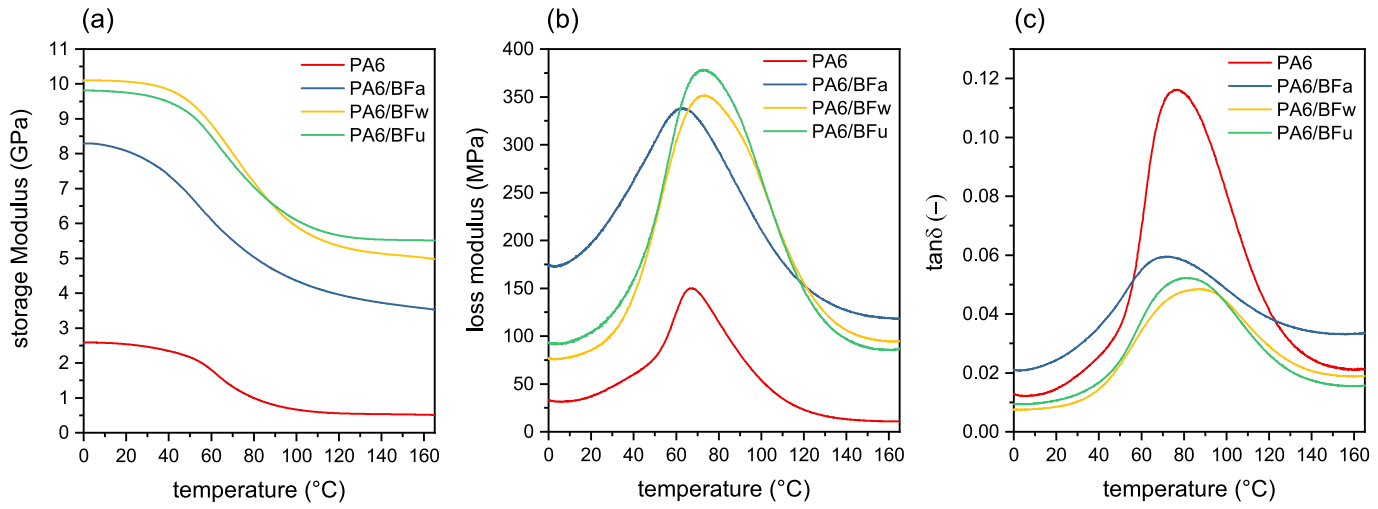

Fig. 8. DMTA thermograms of the prepared composites and the neat PA6 matrix. (a) Storage modulus; (b) loss modulus; (c) loss factor (tanδ).

slightly higher fiber volume fraction (see Table 3) and crystallinity (for PA6/BFu). Moreover, neat PA6 and the sample PA6/BFu seem to show a narrower tanδ peak, and neat PA6 also exhibits a very shallow low-temperature shoulder, implying the presence of an additional transition, which seems to be suppressed in the composite. Although the mechanisms underlying the slightly different viscoelastic behavior of the prepared composites are yet to be fully understood, this test highlights that, for all the studied samples, the glass transition region is consistent with a fully polymerized PA6 with a high degree of conversion and no major influence from the type of reinforcement.

Hence, the results of TGA, DSC, and DMTA tests demonstrate that the surface status of the fibers does not influence considerably the properties of the matrix. Therefore, all the differences in the mechanical and interfacial performance of PA6/BFa, PA6/BFw, and PA6/BFu can be mostly attributed to a variation in the fiber/matrix interfacial adhesion.

The mechanical properties of the PA6/BF composites were evaluated using three-point bending tests. Fig. 9a shows representative stress–strain curves for the prepared composites, calculated in the mid-lower portion of the specimen, subjected to the maximum tensile stress. Fig. 9b summarizes the flexural modulus (E), maximum flexural stress (σ_{fM}), and strain at failure (ε_{fb}) for each sample.

For the neat PA6/BF laminate, the stress increases up to a maximum and then decreases until failure, occurring at a strain of approx. 6 %. Although the standard ASTM D790 suggests stopping the test at 5 %, it was decided to continue the test until 7 % to discriminate between the behavior of PA6/BFa and PA6/BFw, which behaves qualitatively very similar to PA6/BFa but does not break under a strain of 7 %. On the other hand, PA6/BFu displays a brittle behavior, failing abruptly just after

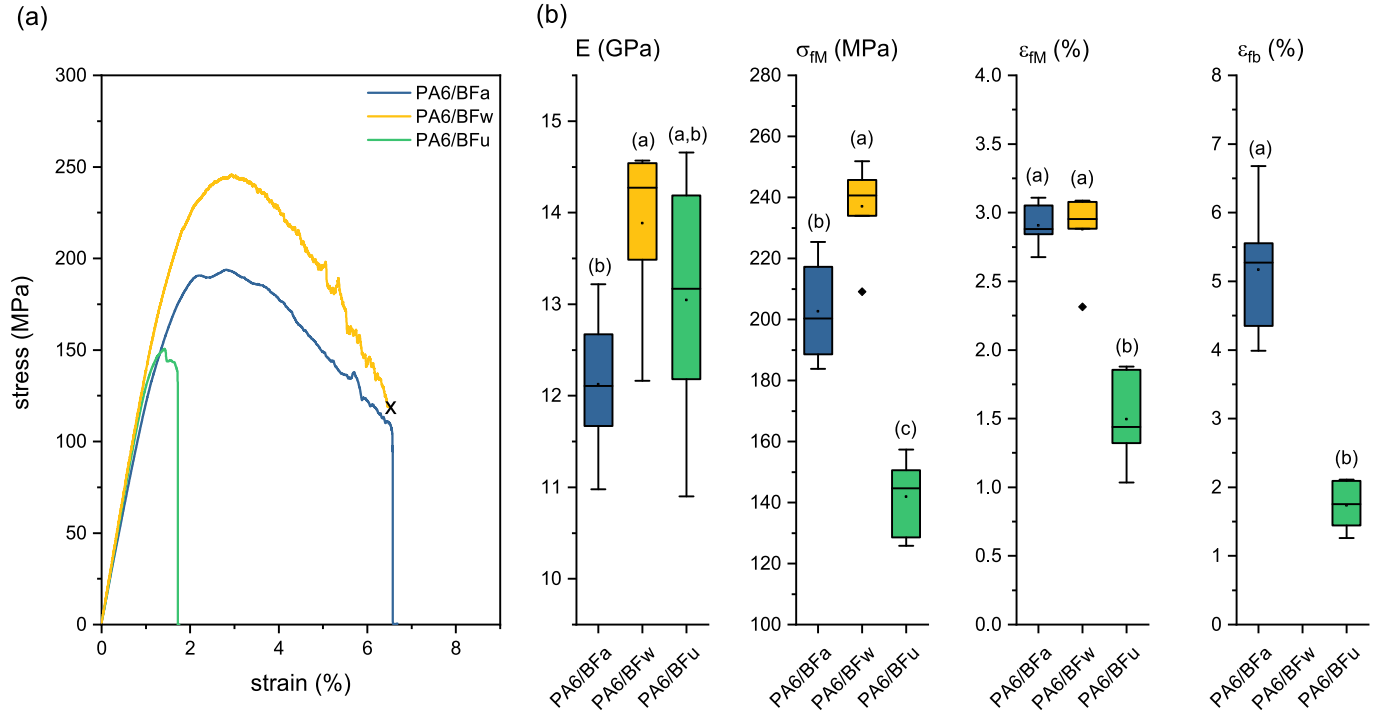

Fig. 9. Main results of the three-point bending tests on the prepared composites. (a) Representative flexural stress–strain curves; (b) flexural modulus (E_f), strength (σ_{fM}), strain at maximum load (ε_{fM}), and strain at break (ε_{fb}). The value of ε_{fb} for the composite PA6/BFw cannot be reported because the specimens did not break during the test. Letters in brackets represent the results of the Tukey HSD test (the same letter means no significant difference).

surpassing the maximum load. This is due to a decreased fiber/matrix interfacial interaction, but it could also be partially caused by a decrease in the strength of the BF after the thermal treatment, as well documented in the literature [15,48]. The same works show, however, that the elastic modulus of BF is not expected to decrease after the thermal treatment. This is likely also the case of this work, as all the prepared composites show an elastic modulus rather close to the theoretical ones, calculated via the rule of mixtures from the tensile modulus of the as-received fibers and the matrix (2.8 GPa [40]) and the measured fiber volume fraction. The theoretical values are generally overestimated, being 13.0 GPa for PA6/BFa, 14.2 GPa for PA6/BFw, and 14.5 GPa for PA6/BFu, with discrepancies attributed to factors such as insufficient span-to-depth ratio during testing, void content, and assumptions of perfect fiber–matrix adhesion in the theoretical model. Finally, it is also interesting to observe that ethanol washing significantly increases the mechanical properties of the laminate, since PA6/BFw has significantly higher elastic modulus and flexural strength than PA6/BFa. This discrepancy may also be partially attributed to the difference in void concentration, higher in the sample PA6/BFa. The obtained mechanical properties are comparable or in some cases even higher than those reported by Rong et al for PA6/BF laminates produced by film stacking and compression molding.

3.3. Investigation of the fiber/matrix interfacial adhesion

The role of the interfacial adhesion between the BF and the PA6 matrix was more closely investigated via three techniques, namely the short beam shear (SBS), fiber push out (FPO), and fiber microdebonding (FMD) tests. Fig. 10 shows representative load–displacement curves obtained in SBS tests, from which the short-beam shear strength is calculated by considering the first local maximum, associated with the first failure event. Since this event was, for all specimens, delamination, the calculated short beam shear strength actually corresponds to the interlaminar shear strength (ILSS). PA6/BFw exhibited the highest ILSS (51.9 ± 8.2 MPa) (Fig. 15), while PA6/BFa showed a slightly lower ILSS (45.5 ± 3.2 MPa), attributed to a lower fiber/matrix adhesion, an effect of impurities that favor defects initiation and propagation, and a higher void content. However, the ANOVA did not highlight significant differences between the two composites. Finally, PA6/BFu demonstrated the lowest ILSS (19.6 ± 1.2 MPa), confirming the crucial role of sizing in interfacial and matrix-dominated properties for this type of composites.

The obtained ILSS values measured on PA6/BFa and PA6/BFw were comparable with those reported in the literature for other composites

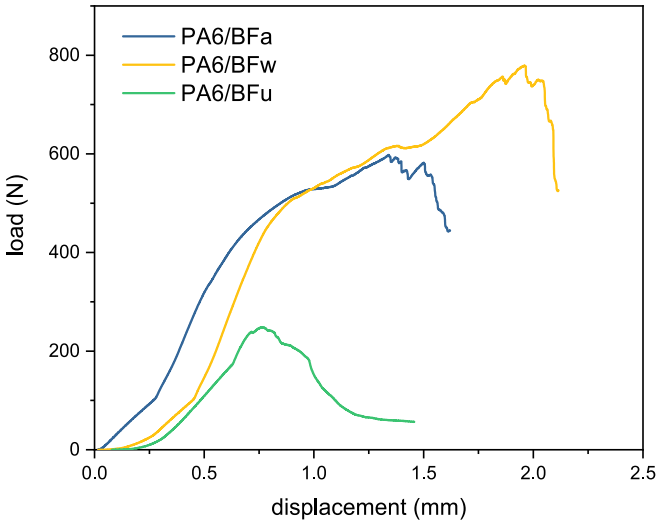

Fig. 10. Representative load–displacement curves obtained in short-beam shear test on the prepared composites.

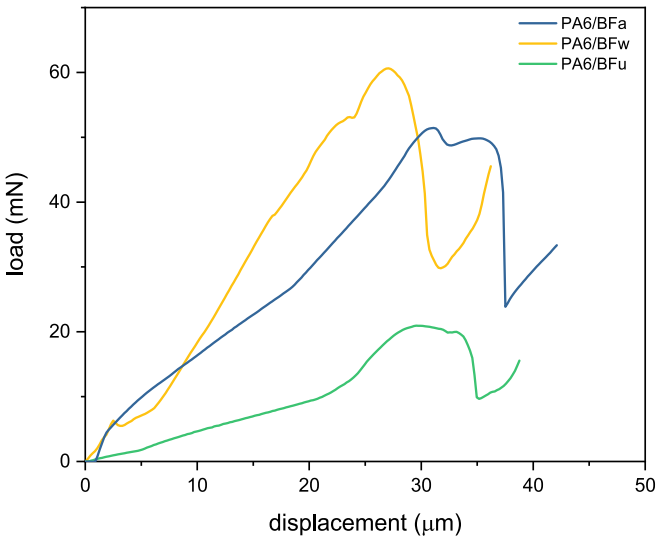

Fig. 11. Representative load–displacement curves obtained in fiber push-out test on the prepared composites.

with an anionic PA6 matrix and carbon [33] or glass [31,32] fibers with traditional sizing, while no comparison was found with anionic PA6/basalt fibers as, to the best of the author's knowledge, there are no previous examples of such composites in the open scientific literature. By comparing the obtained values with those measured by traditional thermoplastic processing, it can be observed that the obtained values are similar to or higher than those reported by Rong et al. [57] for PA6/BF laminates produced by film stacking and compression molding. These authors reported values of short beam shear strength of approx. 20 MPa for neat PA6/BF laminates, which was increased up to approx. 37 MPa after grafting graphene oxide via silane chemistry.

Since the values of the SBS test do not only reflect the interfacial adhesion but also the overall state of the composite in terms of void concentration and fiber alignment, fiber push-out and fiber microdebonding tests were also carried out, to assess interfacial adhesion at the single-fiber level. Fig. 11 presents representative force–displacement curves obtained during the test and Fig. 12 shows a representative specimen of PA6/BFa before and after push-out.. Also in this case, PA6/BFu exhibits the lowest strength (4.2 ± 2.7 MPa) due to the absence of sizing. PA6/BFa and PA6/BFw show similar results, with PA6/BFw displaying the highest interfacial strength (34 ± 11 MPa). The push-out test results are generally lower than those obtained from the SBS test and show higher standard deviations, although a much higher number of data points were taken in this test compared to the SBS test (at least 30 vs. at least 5). The higher variance of micromechanical tests such as pull-out, push-out, and microdebonding compared to tests such as the SBS test is well documented in the literature and is generally attributed to small specimen sizes and neglected local effects [58–60]. For example, a reported source of scattering in FPO tests is the constraining effect of surrounding fibers [61], which is not fully accounted for in existing analytical models. Also, these micromechanical tests depend more heavily than macro-mechanical tests on assumptions about the stress state, fiber geometry, and failure mechanisms. Deviations from these assumptions can introduce scatter [62,63].

In any case, the found push-out strength values for BFa and BFw are similar to those obtained by Haspel et al. [34] between in situ polymerized anionic PA6 and sized glass fiber composites. Those authors found an average interfacial shear strength of 27.2 MPa and considerable variability in the measurements, with individual sample averages ranging from 10 to 41 MPa. The authors attributed the relatively poor interfacial properties to several factors. Polarized light microscopy revealed irregular crystallization of the polyamide 6 matrix near the

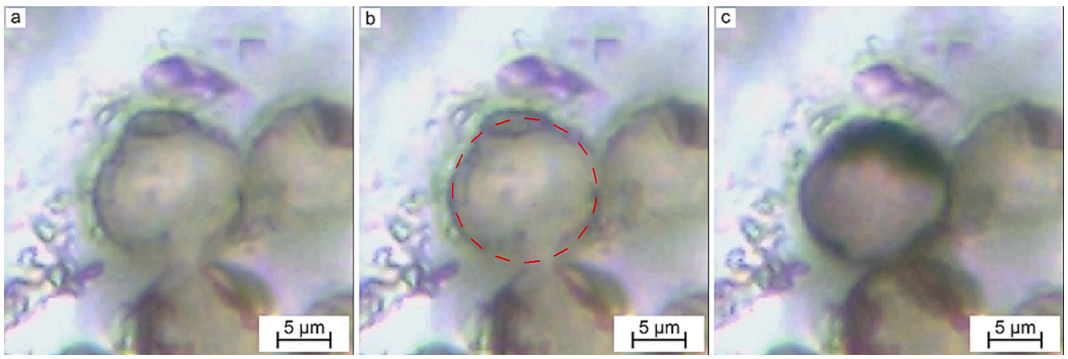

Fig. 12. Representative pictures of the top view of a specimen of PA6/BFa during fiber push-out. (a) Before the test; (b) identification of the fiber perimeter and diameter; (c) after the test.

fibers, with significantly lower crystallinity in densely packed fiber areas. This suggested that the coupling agent used on the glass fibers may not have been fully compatible with the thermoplastic matrix system. The high porosity and fiber volume fraction may also have weakened the interfacial region. SEM analysis of pushed-out fibers showed clean fiber surfaces with no adhered matrix residue, indicating that failure occurred at the fiber-coupling agent interface rather than in the bulk matrix. All these phenomena may have also occurred in this work.

Finally, the results of microdebonding tests are shown in Fig. 13, Fig. 14, and Fig. 15. Because of the very difficult preparation process and the far-from-ideal although interesting first results, this test was carried out only on one type of basalt fibers, i.e., BFw, because it was the fiber type that yielded the highest interfacial adhesion and the best mechanical properties of the composites in the previous tests.

The developed droplet deposition method yielded the successful formation of microdroplets onto the length of the BF, and several droplets could be deposited onto each fiber. This is a fundamental aspect for the subsequent microdebonding test and data analysis with the FIBRObond equipment described in Section 2.3.2. Moreover, DSC and TGA tests on the droplets (Fig. S3, Table S2) confirm the successful polymerization of PA6 and the high degree of conversion. However, the produced droplets show considerable porosity and irregularities (Fig. 13), with cracks and inhomogeneities in both the meniscus zone and the central part of the droplet. This peculiar microstructure is likely caused by the concurrence of polymerization and crystallization. The selected parameters for droplet formation enhance massive polymer

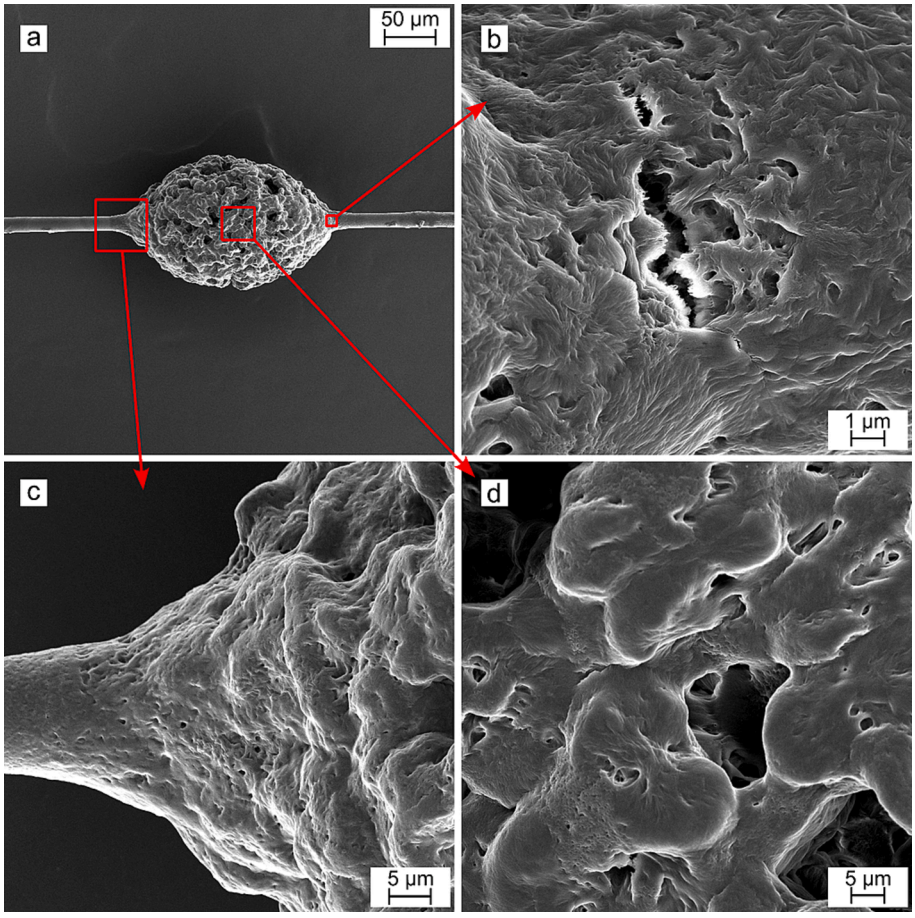

Fig. 13. SEM micrograph of a droplet of PA6 polymerized onto a basalt fiber. (a) Overview of the droplet; (b) detail of a crack in the meniscus zone; (c) detail of the meniscus zone; (d) detail of the central part of the droplet, with evidence of the spherulitic morphology.

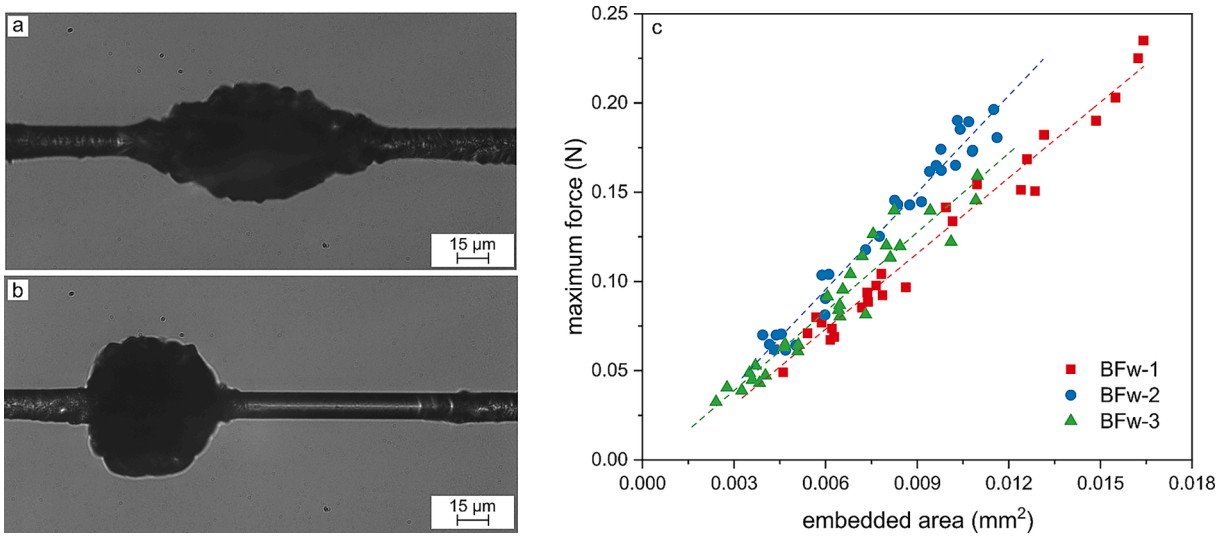

Fig. 14. Results of the microdebonding test. Light microscope micrographs of the droplets before (a) and after (b) the test. (c) maximum force as a function of the embedded area for all the droplets debonded from three basalt fibers.

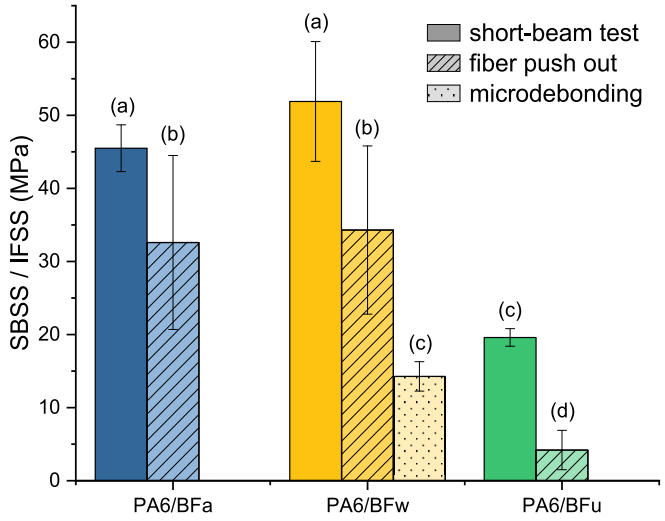

Fig. 15. Results of the fiber/matrix interfacial adhesion tests on the prepared composites. Data of short beam shear strength (SBSS) or interfacial shear strength (IFSS). Data of microdeobonding is the average of all the droplets tested on three different fibers (approx. 30 droplets per fiber). Letters in brackets represent the results of the Tukey HSD test (the same letter means no significant difference).

crystallization (up to 60.7 %, see Table S2), which promotes shrinkage during droplet polymerization. This effect, combined with the lack of monomer supply around the droplet, which is instead common for bulk polymerization, and the probable partial monomer evaporation, is likely at the basis of the particular morphology depicted in Fig. 13. The obtained microstructure and crystallinity resemble those described by Rahman et al. [64], who produced highly crystalline, porous PA6 granules in a solvent-based process, so in a similar condition of lack of monomer reservoir around the developing PA6 crystals.

This microstructure is likely at the basis of the lower IFSS values obtained in this test compared to SBT and push-out tests. Although the high porosity may suggest an overestimation of the fiber-droplet contact surface, this is likely not the cause in this work. This effect would add considerable data scattering, which is not found in the obtained data ($R^2 > 0.98$). Instead, the lower IFSS is likely due to the presence of moisture and residual caprolactam, which may contribute to the high droplet compliance appreciable by observing the shape of the droplet before and after the test (Fig. 14a). This discrepancy may also be ascribed to the nature of the measurement itself, as reported by Herrera-Franco and Drzal [27], since the microdebonding test does not consider stress distribution in the real composite, although the difference between microdebonding and SBS results in this study is higher than the ~50 % difference reported in [27].

Such results are lower than those obtained by Revol et al. with sized glass fibers [37], the only previous example of microdebonding with in situ polymerized PA6 microdroplets, to the best of the authors' knowledge. Although some experimental details of that work remain obscure and SEM micrographs of the droplets were not shown, which makes a full comparison very challenging, those authors report a microdebonding interfacial strength of 20 ± 3 MPa (average of 7 droplets) with in situ polymerized droplets, not significantly different from the 25 ± 6 MPa obtained with melted PA6 droplets. Revol et al., who did not report any observations of porosity in the prepared droplets but only mentioned the imperfect symmetry, used the same polymerization temperature and the same catalysts employed in this work, but in approx. doubled amount. Perhaps the higher amount of catalysts promoted polymerization over crystallization during the droplet formation, although the reported conversion rate is approx. 70 %, much lower than that obtained in this work (82 % minimum, see Table S2).

4. Conclusions

The present study investigated the thermomechanical properties and the fiber/matrix interfacial adhesion in in-situ polymerized anionic polyamide 6 (PA6) composites reinforced with basalt fibers (BF) through a comprehensive multi-technique approach. The influence of the BF surface treatment, namely as-received (BFa), ethanol-washed (BFw), and thermally-desized at 400 °C (BFu), was systematically evaluated. The characterization of the PA6/BF composites highlighted the critical role of the fiber surface state on the interfacial adhesion. The composites with as-received (PA6/BFa) and ethanol-washed (PA6/BFw) BF exhibited enhanced fiber–matrix interaction, as qualitatively evidenced by the matrix residues observed on the fiber surfaces after fracture. In contrast, the thermally-desized composite (PA6/BFu) displayed clean fiber surfaces and prevalent fiber pullout, indicating weaker interfacial bonding. These results were almost entirely ascribed to the different interfacial strength and not to a variation in the properties of the anionic PA6 matrix, which were found marginally affected by the BF surface state.

The quantitative assessment of the interfacial adhesion through short-beam shear, fiber push-out, and microdebonding tests corroborated these findings. The PA6/BFw composite exhibited the highest interfacial shear strength of 51.9 ± 8.2 MPa in the short-beam shear test, followed by PA6/BFa at 45.5 ± 3.2 MPa, while PA6/BFu showed a significantly lower value of 19.6 ± 1.2 MPa. The fiber push-out test yielded similar trends, with PA6/BFw displaying the highest interfacial shear strength of 34 ± 11 MPa, compared to 12 ± 3 MPa for PA6/BFu. The microdebonding test, performed only on the PA6/BFw composite, resulted in a lower interfacial shear strength of 12 ± 4 MPa, likely due to the peculiar morphology of the PA6 droplets characterized by high porosity and irregularities. The discrepancies between the three test methods were attributed to the different scales and stress states probed, highlighting the complementary nature of the employed techniques. The microdebonding test results were also adversely affected by the droplet morphology and microstructure, which modified the mechanical response of the droplets and likely influenced the measured interfacial shear strength.

In conclusion, this study demonstrated the critical importance of the BF surface treatment in determining the fiber–matrix adhesion in in-situ polymerized anionic PA6 composites. The ethanol washing treatment emerged as an effective and simple approach to enhance the mechanical and interfacial properties, with a significantly higher modulus and strength (as measured in three-point bending tests) and a 14 % increase in the short-beam shear strength compared to the as-received fibers, although this difference was not statistically significant. In contrast, thermal desizing halved the IFSS. The multi-technique characterization provided a comprehensive understanding of the interfacial behavior in these novel thermoplastic composites, paving the way for the application of such composites in high-end fields.

These findings have broader implications for the design and optimization of high-performance thermoplastic composites reinforced with natural or mineral fibers. The ability to tailor the fiber–matrix interface through simple surface treatments, by leaving the bulk matrix properties almost intact, is crucial for unlocking the full potential of these sustainable and lightweight materials. By understanding the complex interplay between fiber surface chemistry, matrix crystallization, and interfacial adhesion, strategies can be developed to enhance the mechanical and thermal properties of these composites, ultimately expanding their application range. Hence, future work should focus on further optimizing the fiber surface treatments and the in-situ polymerization conditions to achieve an optimized fiber–matrix bond. Exploring alternative coupling agents or compatibilizers that can effectively bridge the gap between the polar basalt fibers and the non-polar PA6 matrix may lead to additional improvements in interfacial adhesion. Additionally, investigating the long-term durability and environmental resistance of these composites as a function of the BF surface state and under various service conditions will be essential for assessing their viability for real-world applications.

CRediT authorship contribution statement

Martino Valentini: Visualization, Investigation, Formal analysis. **Olivier De Almeida:** Writing – review & editing, Validation, Supervision, Resources, Methodology, Investigation, Conceptualization. **Markus Kakkonen:** Writing – review & editing, Investigation, Formal analysis. **Gerhard Kalinka:** Writing – review & editing, Investigation, Formal analysis. **Andrea Dorigato:** Writing – review & editing, Supervision, Project administration, Funding acquisition. **Pasi Kallio:** Resources. **Giulia Fredi:** Writing – review & editing, Writing – original draft, Visualization, Validation, Supervision, Project administration, Methodology, Investigation, Formal analysis, Data curation, Conceptualization.

Funding

The work has been produced with the co-funding of the European Union, FSE-REACT-EU, PON Research and Innovation (Action IV.6 - Green) 2014-2020 DM1062/2021.

Declaration of competing interest

The authors declare the following financial interests/personal relationships which may be considered as potential competing interests: Giulia Fredi reports financial support was provided by European Union. If there are other authors, they declare that they have no known competing financial interests or personal relationships that could have appeared to influence the work reported in this paper.

Acknowledgments

L. Brüggemann GmbH & Co. KG is kindly acknowledged for providing the monomer and catalysts. Mr. Damien Gacon and Mr. Vincent Lucin are gratefully acknowledged for their support in the preparation of the samples for the microdebonding test and the SEM observations of the microdebonding specimens. Mr. Lorenzo Broggio, Mr. Tommaso Eccher, and Dr. Daniele Rigotti are gratefully acknowledged for their support in the preparation of the composites. Ms. Claudia Gavazza and Mr. Alfredo Casagranda are gratefully acknowledged for their support to the experimental activities.

Appendix A. Supplementary data

Supplementary data to this article can be found online at https://doi.org/10.1016/j.compositesa.2024.108681.

Data availability

Data will be made available on request.

References

[1] Valente M, Rossitti I, Biblioteca I, Sambucci M. Thermoplastic composite materials approach for more circular components: from monomer to in situ polymerization, a review. J Compos Sci 2022;6(5):132. https://doi.org/10.3390/jcs6050132.
[2] van Rijswijk K, Bersee HEN. Reactive processing of textile fiber-reinforced thermoplastic composites – an overview. Compos A Appl Sci Manuf 2007;38(3):666–81. https://doi.org/10.1016/j.compositesa.2006.05.007.
[3] Belkhiri A, Virgilio N, Santanach-Carreras E, Esvan J, Nassiet V, Welemane H, et al. Influence of silane interfacial chemistry on the curing process of anionic Polyamide 6 in glass reinforced composites. Colloids Surf A Physicochem Eng Asp 2023;676:132183. https://doi.org/10.1016/j.colsurfa.2023.132183.
[4] Sun L, Cao M, Xiao F, Xu J, Chen Y. POSS functionalized graphene oxide nanosheets with multiple reaction sites improve the friction and wear properties of polyamide 6. Tribol Int 2021;154:106747. https://doi.org/10.1016/j.triboint.2020.106747.
[5] Ageyeva T, Sibikin I, Kovacs JG. A review of thermoplastic resin transfer molding: process modeling and simulation. Polymers (Basel) 2019;11(10):1555. https://doi.org/10.3390/polym11101555.
[6] Durai Prabhakaran RT. Are reactive thermoplastic polymers suitable for future wind turbine composite materials blades? Mech Adv Mater Struct 2013;21(3):213–21. https://doi.org/10.1080/15376494.2013.834090.
[7] Qin Y, Summerscales J, Graham-Jones J, Meng M, Pemberton R. Monomer selection for in situ polymerization infusion manufacture of natural-fiber reinforced thermoplastic-matrix marine composites. Polymers (Basel) 2020;12(12):2928. https://doi.org/10.3390/polym12122928.
[8] Sibikin I, Karger-Kocsis J. Toward industrial use of anionically activated lactam polymers: past, present and future. Adv Ind Eng Polym Res 2018;1(1):48–60. https://doi.org/10.1016/j.aiepr.2018.06.003.
[9] Dubois P, Coulembier O, Raquez J-M. Handbook of ring-opening polymerization. Weinheim, Germany: WILEY-VCH Verlag GmbH & Co. KGaA; 2009.
[10] Vicard C, De Almeida O, Cantarel A, Bernhart G. Experimental study of polymerization and crystallization kinetics of polyamide 6 obtained by anionic ring opening polymerization of ε-caprolactam. Polymer 2017;132:88–97. https://doi.org/10.1016/j.polymer.2017.10.039.
[11] Scheffler C, Förster T, Mäder E, Heinrich G, Hempel S, Mechtcherine V. Aging of alkali-resistant glass and basalt fibers in alkaline solutions: evaluation of the failure

stress by Weibull distribution function. J Non Cryst Solids 2009;355(52–54): 2588–95. https://doi.org/10.1016/j.jnoncrysol.2009.09.018.
[12] Greco A, Maffezzoli A, Casciaro G, Caretto F. Mechanical properties of basalt fibers and their adhesion to polypropylene matrices. Compos B Eng 2014;67:233–8. https://doi.org/10.1016/j.compositesb.2014.07.020.
[13] Lilli M, Acauan L, Scheffler C, Tirillò J, Guzmánde Villoria R, Wardle BL, et al. Low temperature direct growth of carbon nanostructures on basalt fibers. Compos B Eng 2023;262. https://doi.org/10.1016/j.compositesb.2023.110826.
[14] Szakács J, Mészáros L. Synergistic effects of carbon nanotubes on the mechanical properties of basalt and carbon fiber-reinforced polyamide 6 hybrid composites. J Thermoplast Compos Mater 2017;31(4):553–71. https://doi.org/10.1177/0892705717713055.
[15] Lu Z, Xian G. Resistance of basalt fibers to elevated temperatures and water or alkaline solution immersion. Polym Compos 2016;39(7):2385–93. https://doi.org/10.1002/pc.24220.
[16] Torres JP, Hoto R, Andrés J, García-Manrique JA. Manufacture of green-composite sandwich structures with basalt fiber and bioepoxy resin. Adv Mater Sci Eng 2013; 2013:1–9. https://doi.org/10.1155/2013/214506.
[17] Pucci MF, Seghini MC, Liotier P-J, Sarasini F, Tirilló J, Drapier S. Surface characterisation and wetting properties of single basalt fibres. Compos B Eng 2017; 109:72–81. https://doi.org/10.1016/j.compositesb.2016.09.065.
[18] Narayanan A, Shanmugasundaram P. Evaluation of heat resisting behaviour of basalt fibre reinforced FG tiles. Constr Build Mater 2018;170:679–89. https://doi.org/10.1016/j.conbuildmat.2018.03.110.
[19] Chen C, Ding Y, Wang X, Bao L. Recent advances to engineer tough basalt fiber reinforced composites: A review. Polym Compos 2024;45(14):12559–74. https://doi.org/10.1002/pc.28711.
[20] Jagadeesh P, Rangappa SM, Siengchin S. Basalt fibers: an environmentally acceptable and sustainable green material for polymer composites. Constr Build Mater 2024;436. https://doi.org/10.1016/j.conbuildmat.2024.136834.
[21] Khandelwal S, Rhee KY. Recent advances in basalt-fiber-reinforced composites: Tailoring the fiber-matrix interface. Compos B Eng 2020;192. https://doi.org/10.1016/j.compositesb.2020.108011.
[22] Dorigato A, Pegoretti A. Fatigue resistance of basalt fibers-reinforced laminates. J Compos Mater 2012;46(15):1773–85. https://doi.org/10.1177/0021998311425620.
[23] Alfonso A, Andrés J, García JA. Study of the proper sintering conditions of anionically-polymerized polyamide 6 matrices for the fabrication of greencomposites. Mater Sci Forum 2012;713:121–6. https://doi.org/10.4028/www.scientific.net/MSF.713.121.
[24] Alfonso A, Andrés J, García-Manrique JA. Synthesis of APA6 thermoplastic matrices for the manufacture of greencomposites. In: Physics AIo, editor. The 4th Manufacturing Engineering Society International Conference (MESIC 2011); 2012. p. 778–87.
[25] Wilhelm M, Wendel R, Aust M, Rosenberg P, Henning F. Compensation of water influence on anionic polymerization of ε-caprolactam: 1. chemistry and experiments. J Compos Sci 2020;4(1):7. https://doi.org/10.3390/jcs4010007.
[26] AhmadvashAghbash S, Verpoest I, Swolfs Y, Mehdikhani M. Methods and models for fibre–matrix interface characterisation in fibre-reinforced polymers: a review. Int Mater Rev 2023;68(8):1245–319. https://doi.org/10.1080/09506608.2023.2265701.
[27] Herrera-Franco PJ, Drzal LT. Comparison of methods for the measurement of fibre/matrix adhesion in composites. Composites 1992;23(1):2–27.
[28] Morlin B, Czigany T. Cylinder test: development of a new microbond method. Polym Test 2012;31(1):164–70. https://doi.org/10.1016/j.polymertesting.2011.10.007.
[29] Huang S, Fu Q, Yan L, Kasal B. Characterization of interfacial properties between fibre and polymer matrix in composite materials – a critical review. J Mater Res Technol 2021;13:1441–84. https://doi.org/10.1016/j.jmrt.2021.05.076.
[30] Fredi G, Dorigato A, Unterberger S, Artuso N, Pegoretti A. Discontinuous carbon fiber/polyamide composites with microencapsulated paraffin for thermal energy storage. J Appl Polym Sci 2019;136(16):47408/1-47408/14. https://doi.org/10.1002/app.47408.
[31] van Rijswijk K, van Geenen AA, Bersee HEN. Textile fiber-reinforced anionic polyamide-6 composites part II: investigation on interfacial bond formation by short beam shear test. Compos A Appl Sci Manufac 2009;40(8):1033–43. https://doi.org/10.1016/j.compositesa.2009.02.018.
[32] Teuwen JJE, van Geenen AA, Bersee HEN. Vacuum-infused anionic polyamide-6 composites: the effect of postprocessing. J Thermoplast Compos Mater 2011;25(8): 965–86. https://doi.org/10.1177/0892705711415739.
[33] Shim YB, Park YB. Development of single-stream resin transfer molding using in-situ anionic polymerization of ε-caprolactam with preprocessing on carbon fibers. Polym Compos 2024;45(9):8296–305. https://doi.org/10.1002/pc.28341.
[34] Haspel B, Hoffmann C, Elsner P, Weidenmann KA. Characterization of the interfacial shear strength of glass-fiber reinforced polymers made from novel RTM processes. Int J Plast Technol 2016;19(2):333–46. https://doi.org/10.1007/s12588-015-9122-3.
[35] Sun N, Zhu B, Cai X, Yu L, Yuan X, Zhang Y. Enhanced interfacial properties of carbon Fiber/Polyamide composites by In-situ synthesis of polyamide 6 on carbon fiber surface. Appl Surf Sci 2022;599. https://doi.org/10.1016/j.apsusc.2022.153889.
[36] Tohidi SD, Rocha AM, Dourado N, Rezazadeh M, Quyền NT, Zille A, et al. Influence of transcrystalline layer on finite element mesoscale modeling of polyamide 6 based single polymer laminate composites. Compos Struct 2020;232. https://doi.org/10.1016/j.compstruct.2019.111555.
[37] Revol BP, Thomassey M, Ruch F, Bouquey M, Nardin M. Single fibre model composite: interfacial shear strength measurements between reactive polyamide-6 and cellulosic or glass fibres by microdroplet pullout test. Compos Sci Technol 2017;148:9–19.
[38] Osváth Z, Szőke A, Pásztor S, Szarka G, Závoczki LB, Iván B. Post-polymerization heat effect in the production of polyamide 6 by bulk quasiliving anionic ring-opening polymerization of ε-caprolactam with industrial components: a green processing technique. Processes 2020;8(7):856. https://doi.org/10.3390/pr8070856.
[39] Lagarinhos J, Santos L, Oliveira J. Effect of catalyst and activator on properties of polyamide 6 prepared by thermoplastic resin transfer molding technology. J Mater Eng Perform 2022;31(9):7098–103. https://doi.org/10.1007/s11665-022-07044-4.
[40] Fredi G, Broggio L, Valentini M, Bortolotti M, Rigotti D, Dorigato A, et al. Decoding the interplay of mold temperature and catalysts concentration on the crystallinity and mechanical properties of anionic polyamide 6: a combined experimental and statistical approach. Polymer 2024. https://doi.org/10.1016/j.polymer.2024.127562.
[41] Humphry J, Yang N, Vandi LJ, Hernandez BV, Martin DJ, Heitzmann MT. Isothermal differential scanning calorimetry analysis of the anionic polymerisation of polyamide-6: Separation by dual asymmetric gaussians. Mater Today Commun 2020;25:101473. https://doi.org/10.1016/j.mtcomm.2020.101473.
[42] Gebhardt M, Manolakis I, Chatterjee A, Kalinka G, Deubener J, Pfnür H, et al. Reducing the raw material usage for room temperature infusible and polymerisable thermoplastic CFRPs through reuse of recycled waste matrix material. Compos B Eng 2021;216. https://doi.org/10.1016/j.compositesb.2021.108877.
[43] Laurikainen P, Kakkonen M, Essen Mv, Tanhuanpää O, Kallio P, Sarlin E. Identification and compensation of error sources in the microbond test utilising a reliable high-throughput device. Compos A Appl Sci Manuf 2020;17:105988. https://doi.org/10.1016/j.compositesa.2020.105988.
[44] Samper MD, Petrucci R, Sánchez-Nacher L, Balart R, Kenny JM. Effect of silane coupling agents on basalt fiber-epoxidized vegetable oil matrix composite materials analyzed by the single fiber fragmentation technique. Polym Compos 2015;36(7):1205–12. https://doi.org/10.1002/pc.23023.
[45] Iorio M, Santarelli ML, González-Gaitano G, González-Benito J. Surface modification and characterization of basalt fibers as potential reinforcement of concretes. Appl Surf Sci 2018;427:1248–56. https://doi.org/10.1016/j.apsusc.2017.08.196.
[46] Pickering KL, Murray TL. Weak link scaling analysis of high-strength carbon fibre. Compos A 1999;30:1017–21.
[47] Paramonov Y, Andersons J. A family of weakest link models for fiber strength distribution. Compos A Appl Sci Manuf 2007;38(4):1227–33. https://doi.org/10.1016/j.compositesa.2006.06.004.
[48] Sarasini F, Tirillò J, Seghini MC. Influence of thermal conditioning on tensile behaviour of single basalt fibres. Compos B Eng 2018;132:77–86. https://doi.org/10.1016/j.compositesb.2017.08.014.
[49] Militky J, Kovacic V, Rubnerova J. Influence of thermal treatment on tensile failure of basalt fibers. Eng Fract Mech 2002;69:1025–33.
[50] Ricco L, Russo S, Orefice G, Riva F. Anionic poly(ε-caprolactam): relationships among conditions of synthesis, chain regularity, reticular order, and polymorphism. Macromolecules 1999;32:7726–31. https://doi.org/10.1021/ma9909004.
[51] van Rijswijk K, Bersee HEN, Beukers A, Picken SJ, van Geenen AA. Optimisation of anionic polyamide-6 for vacuum infusion of thermoplastic composites: influence of polymerisation temperature on matrix properties. Polym Test 2006;25(3): 392–404. https://doi.org/10.1016/j.polymertesting.2005.11.008.
[52] Russo S, Imperato A, Mariani A, Parod F. The fast activation of ε-caprolactam polymerization in quasiadiabatic conditions. Macromol Chem Phys 1995;196: 3297–303.
[53] Millot C, Fillot L-A, Lame O, Sotta P, Seguela R. Assessment of polyamide-6 crystallinity by DSC. J Therm Anal Calorim 2015;122(1):307–14. https://doi.org/10.1007/s10973-015-4670-5.
[54] Semperger OV, Suplicz A. The effect of the parameters of T-RTM on the properties of polyamide 6 prepared by in situ polymerization. Materials (Basel) 2019;13(1):4. https://doi.org/10.3390/ma13010004.
[55] Kim SW, Park T, Um MK, Lee J, Seong DG, Yi JW. Effect of caprolactam modified phenoxy-based sizing material on reactive process of carbon fiber-reinforced thermoplastic polyamide-6. Compos A Appl Sci Manuf 2020;139. https://doi.org/10.1016/j.compositesa.2020.106104.
[56] Liang J, Xu Y, Wei Z, Song P, Chen G, Zhang W. Mechanical properties, crystallization and melting behaviors of carbon fiber-reinforced PA6 composites. J Therm Anal Calorim 2013;115(1):209–18. https://doi.org/10.1007/s10973-013-3184-2.
[57] Rong Y, Zhao P, Shen T, Gao J, Zhou S, Huang J, et al. Mechanical and tribological properties of basalt fiber fabric reinforced polyamide 6 composite laminates with interfacial enhancement by electrostatic self-assembly of graphene oxide. J Mater Res Technol 2023;27:7795–806. https://doi.org/10.1016/j.jmrt.2023.11.175.
[58] Teuber L, Fischer H, Graupner N. Single fibre pull-out test versus short beam shear test: comparing different methods to assess the interfacial shear strength. J Mater Sci 2013;48(8):3248–53. https://doi.org/10.1007/s10853-012-7107-6.
[59] Yavin B, Wagner HD. Micromechanical measurements of interfacial adhesion in E-glass/epoxy composites. Adv Compos Lett 1993;2(2):47–50. https://doi.org/10.1177/096369359300200 2.
[60] Verpoest I, Desaeger M, Ivens J, Wevers M. Interfaces in polymer matrix composites: from micromechanical tests to macromechanical properties. Makromol

Chem, Macromol Symp 1993;75:85–98. https://doi.org/10.1002/masy.19930750109.
[61] Molina-Aldareguía JM, Rodríguez M, González C, LLorca J. An experimental and numerical study of the influence of local effects on the application of the fibre push-in tests. Philosoph Magaz 2011;91(7-9):1293–307. https://doi.org/10.1080/14786435.2010.480947.
[62] Pisanova E, Zhandarov S, Mader E. How can adhesion be determined from micromechanical tests? Compos A 2001;32:425–34. https://doi.org/10.1016/S1359-835X(00)00055-5.
[63] Zhou XF, Nairn JA, Wagner HD. Fiber–matrix adhesion from the single-fiber composite test: nucleation of interfacial debonding. Compos A 1999;30:1387–400. https://doi.org/10.1016/S1359-835X(99)00043-3.
[64] Rahman MA, Renna LA, Venkataraman D, Desbois P, Lesser AJ. High crystalline, porous polyamide 6 by anionic polymerization. Polymer 2018;138:8–16. https://doi.org/10.1016/j.polymer.2018.01.040.